PCCP

Blue Energy Generation by the Temperature-dependent Properties in Funnel-Shaped Soft Nanochannels

Journal:	*Physical Chemistry Chemical Physics*
Manuscript ID	CP-ART-03-2022-001015.R2
Article Type:	Paper
Date Submitted by the Author:	21-Jul-2022
Complete List of Authors:	Karimzadeh, Mohammad; Iran University of Science and Technology, Chemical Engineering; Khatibi, Mahdi; Iran University of Science and Technology, chemical engineering Ashrafizadeh, Seyed Nezameddin; Iran University of Science and Technology, Chemical Engineering Mondal, Pranab; Indian Institute of Technology Guwahati, Mechanical Engineering

Blue Energy Generation by the Temperature-dependent Properties in Funnel-Shaped Soft Nanochannels

Mohammad Karimzadeh[a], Mahdi Khatibi[a], Seyed Nezameddin Ashrafizadeh[*,a], Pranab Kumar Mondal[b]

[a]*Research Lab for Advanced Separation Processes, Department of Chemical Engineering, Iran University of Science and Technology, Narmak, Tehran 16846-13114, Iran*
[b]*Microfluidics and Microscale Transport Laboratory, Department of Mechanical Engineering, Indian Institute of Technology Guwahati, Assam 781039, India*

Abstract

Salinity energy generation (SEG) studies have only been done under isothermal conditions at ambient temperature. The production of salinity energy can be improved under non-isothermal conditions, albeit preserving the energy efficiency. In the current study, effects gradients of temperature and concentration were examined simultaneously on the salinity energy generation process. Based on the temperature-dependent properties resulting from both temperature and concentration gradients, a numerical study was carried out to determine the maximum efficiency of salinity energy generation in funnel-shaped soft nanochannels. It was presumed that a dense layer of negatively charged, called as polyelectrolyte layer (PEL), is coated on the walls of nanochannel. Co-current and counter-current modes were used to implement temperature and concentration gradients. At steady-state conditions, the Poisson-Nernst-Planck, Stokes-Brinkman, and energy equations were numerically solved by using equivalent approaches. The results revealed that by increasing the temperature and concentration ratios at both co-current and counter-current modes of operation, the salinity energy generation increased appreciably. The salinity energy generation increased from 30 to 80 pW by increasing the temperature ratio from 1 to 8 at constant concentration ratio of 1000 in the counter-current mode. As verified from this analysis, low-grade heat sources (<100 °C) provide considerable energy conversion in a PEL grafted nanofluidic confinements when placed between electrolyte solutions having different temperatures.

Keywords: Soft Nanochannel; Salinity Energy Generation; Reverse Electrodialysis; Osmotic Current; Non-isothermal Condition.

* Corresponding author: ashrafi@iust.ac.ir (S. N. Ashrafizadeh)

Co-authors: mohammad_karimzadeh@chemeng.iust.ac.ir (M. Karimzadeh); m_khatibi@chemeng.iust.ac.ir (M. Khatibi); pranabm@iitg.ac.in (P. K. Mondal)

1. Introduction

Growing demand of non-conventional energy is persistent over the years, attributed primarilly to the threating concern of environmental pollution linked with conventional energy generation from fossil fuels. This aspect compelled researchers to develop several sustainable methods of harvesting non-conventional energy in recent years over disperate scales of system [1-15]. The non-conventional energy generation from sources such as biomass, solar, waves, hydro, wind, and salinity gradient energy, being an important topic in the 21st century, has recevied significant attention as a clean energy sources [16-21]. Among many such soucses, the salinity gradient energy resulting from Gibbs energy of mixing, which is generated by combining liquids that have different concentrations like sea and river water, holds the promising capability of high-potential electricity generation due to its abundance [22, 23]. Today, salinity-gradient reversible electrodialysis (RED) and pressure-retarded osmosis (PRO) provide the best methods of utilizing both technologies [24, 25]. The RED system, which is inherently associated with the miniaturized systems, has received the most attention [26, 27].

When nanochannels/nanopores connect two large tanks containing electrolytes of different concentrations, the salinity-gradient reversible electrodialysis (RED) sets in [28-31]. An electrical charge inside the nanochannels filled with electrolytes causes a change in the electrolyte concentration to neutralize the charge on the surface. This process results in the formation of an electric double layer within the electrolyte and on the nanochannel surfaces, where counter-ions predominate over co-ions [32-34]. Nanochannels act as ionic selective structures on the counter-ions in the electrolyte, while repelling the opposite co-ions due to the formation EDL thickness (1 to 100 nm, which is of the order of channel diameter at the nanoscale) [35-37]. The ion-selective behaviour of channels, coupled with the tendency of ions to migrate between the

high and low concentration reservoirs, results in a net diffusion current. With the use of an external circuit, the diffusion current can be converted to an electric current [38-40].

Concerning with the advancement of RED technology, nanoscale systems are attracting increasing attention to the reserchers primarilly due to their higher power density than conventional systems. To understand how micro-/nanosystems activate as well as promot the RED, researchers have conducted numerous experimental as well as theoretical studies [41]. From the reported literature it is seen that solid-state and cylindrical nanochannels have been favoured in most of the analyses pertinent to this paradigm. Performing experimental investigations, Liu et al. identified a way to make a carbon membrane with $67\ W/m^2$ power density, which is twice the size of the conventional membranes [42]. A maximum conversion efficiency of 45% was obtained using three types of salts modelled by Yeh et al using ion-selective conical-shaped nanopores [43]. A study conducted by Kim et al. [44] used a nanoscale porous silica and KCl electrolyte to create power from silica, and resulting in a power density of $7.7\ \mathrm{W/m^2}$. Kim et al. [45] claimed that they were able to produce 543 nW of energy from nanopores with a mean pore radius of 10 nm using NaCl solutions in alumina. Using alumina nanopores, through extensive finite-element-based numerical simulations, Kang et al. [22] were also able to obtain energy densities of up to $9.9\ \mathrm{W/m^2}$.

There are many factors that may affect RED performance, such as concentration ratio, temperature ratio, electrolyte nature, geometry of nanopores and nanochannels, pH, surface properties, and surface charge density [11, 46-51]. Due to the dependence of surface phenomena on wall properties, researchers are interested in figuring out ways to manipulate the surface to achieve desired characteristics. For the purpose of regulating interfacial interactions, in many situations, a penetrable polyelectrolyte layer (PEL), also known as the soft layer, is applied

to the walls of nanochannels [52-57]. Polyelectrolyte layer is frequently utilized to change the surface of inorganic and organic nanochannels, so imparting them with a versatile quality and, consequently, an ICR nature. For instance, Zhang et al.[58] discovered that a glass conical nanopore modified by poly[2-(dimethylamino)ethyl methacrylate], a smart homopolymer capable of undergoing conformational transitions triggered by pH and temperature, exhibited ICR behavior. Umehara et al. [59] demonstrated that a nanopipette coated with poly-L-lysine can enhance ionic current and provide rectification in the opposite direction of an uncoated nanopipette. Deng et al. [60] discovered, in an investigation of the ICR of a glass nanopipette coated with PEI, that its rectification factor has a local maximum as the bulk salt concentration varies, regardless of the presence of a salt gradient. The coating of materials on a nanopore also allows for the estimation of the pKa of the coating materials via the experimentally determined pH–ionic current relationship. Liu et al. [61] measured the pKa of polyethyleneimines (PEIs) by depositing them on a glass nanopipette. For energy production applications Khatibi et al. [62] reported that conical soft nanochannels could produce power output densities of up to 51.5% when KCl concentration gradients were applied along the nanochannel. In a separate study, the same authors obtained a power density of $75\,\mathrm{W/m^2}$, by considering the ion partitioning properties for cone-shaped soft nanochannels [63].

However, previous studies of the SEG process, as reported in the referred literature, are restricted to an isothermal operating condition. It is common as well as intutive to maintain the operating temperature at the same level as the ambient temperature. As such, systems have never been examined in conjunction with varying operating temperatures [5, 64]. When a temperature gradient is imposed across a nanochannel, ions tend to mitigate from the hot to cold region due to the Soret effect, which is inherently responsive to such gradients [65-67]. When ion transport in nano and microchannels is driven by thermal gradients, the effect is actually

similar to streaming potential, which can be measured using the principle of Soret effect essentially to analyze the effect of ionic motion during temperature gradients [1]. Long et al. have shown that a counter-diffusion temperature gradient enhances the membrane potential and the electrical efficiency of thermally insulated nanochannels, thus enhancing ion selectivity [5, 68]. Karimzadeh et al., [69] explored that the ion selectivity improves when the temperature- and concentration gradients are applied in opposite directions, mainly attributed to the temperature-dependent properties of ionic transport in conical soft nanochannels.

Nanochannels are produced in a variety of symmetric and asymmetric configurations to give almost realistic models for ion transport. The conical, bullet, trumpet, and cigarette nanochannels have been the focus of a significant amount of study leveraging asymmetries in shape to induce ICR and electrokinetic energy harvesting. This is mostly owing to the fact that, in asymmetric nanochannels, the overlap of EDLs generated on the channel walls changes, hence enhancing the ICR and electrokinetic energy harvesting. In contrast, if EDLs overlap in symmetric nanochannels, the result is a uniform overlap and does not result in rectification [16, 62, 63]. In addition to the influence of geometry on ion transport behavior, it is feasible to make nanochannels sensitive to environmental changes such as variations in temperature, concentration, voltage, and pH by altering their surface. As a consequence, the efficiency of these systems rises, making them a possible future option for producing sustainable energy [17, 70].

Various shapes of nanochannels have been described, including cylindrical, hourglass-shaped, cigar-shaped, bullet-shaped, conical, and dumbbell-shaped nanochannels. Nevertheless, previously described nanochannels, such as conical nanochannels, have just a brief critical zone at the tip, resulting in poor controllability of the orientation and amount of

ionic rectification [17]. To achieve more complex functions, it is required to examine a unique solid-state nanochannel system with a longer critical zone that is precisely controlled by its asymmetric shape. Herein, we modelled nanochannels in the shape of funnels with three components: a conical section, a spout, and a cylindrical segment (Fig. 2b). Compared to conical nanochannels, the funnel-shaped nanochannels display higher asymmetric ion transport capabilities.

In this study, the osmotic current and diffusion potential in funnel-shaped soft nanochannels were thoroughly investigated. For this purpose, we simultaneously solved the Stokes-Brinkman, Poisson-Nernst-Planck, and energy equations following benchmarked numerical methods. A two-mode gradient was examined for the system, namely co-current (the gradients of temperature and concentration take place in the same direction, i.e., type I) and counter-current (the gradients of temperature and concentration take place in opposite directions, i.e., type II). These gradients were further studied for investigating their effects on transference number, osmotic current, diffusion potential, maximum efficiency of salinity energy generation, and the total generated salinity energy.

2. Problem definition

A funnel-shaped soft nanochannel, operated in both modes of type I (co-current mode, i.e., the concentration and temperature gradients are in the same direction) and type II (counter-current mode, i.e., the concentration and temperature gradients are in the opposit direction), is considered in this analysis as schemtiaclly illustrated in Fig. 1. As a result of the prevailimg quasi-steady-state conditions, several functionalities set-in in the nanochannel like the osmotic current, diffusion potential, and the transport of fluid owing to the electroosmotic effect. A dense polyelectrolyte layer (PEL) of particular thickness is coated at the interior/ exterior parts

of the negatively charged walls of the nanochannel [16, 17]. As shown in Fig. 2a, the nanochannel has a funnel-shaped geometry and consisting of a conical and a cylindrical sections. The physical dimensions of the chosen flow configuration are given as follows: length of the conical section: L_{N1}, length of the cylindrical section: L_{N2}, the radius of two equal-size large reservoirs: L_R, the tip and base radius: R_T and R_B, respectively. Addtionally, the width of PEL is considered as R_S. The reservoirs are sufficiently large so that the end effects can be ignored in the undelrying analysis. Taking into account the channel's symmetry around its central axis, the calculations are performed only at the symmetry half portion of the chanel i.e., for half of the nanochannel essentially to minimize the computational time [69]. Two electrodes are placed in the channel, wherein the left electrode functioning as the working electrode, and the right electrode grounding the channel. The gradients of concentration and/or temperature, which is created across the reservoirs in the desired direction, result in an osmotic current to flow through the nanochannel. According to Fig. 2a, the cylindrical coordinate system (r, z, θ) is used for the description of the funnel-shaped nanochannel, with its origin located on the axis of the nanochannel which runs through the left wall of the tank [62].

It should be noted that, depending on the wall surface qualities, a temperature gradient serves as an external field on ionic transfer species in micro/nanochannels and forces the ionic species toward the cold or the warm. We examine the nature of ionic transport in charged nanochannels and how a temperature gradient generates companion fields. Special attention is placed on the thermal response of the electrolyte solution: positive and negative ions travel along the temperature gradient, therefore generating a thermoelectric field that operates on the ionic species [71, 72].

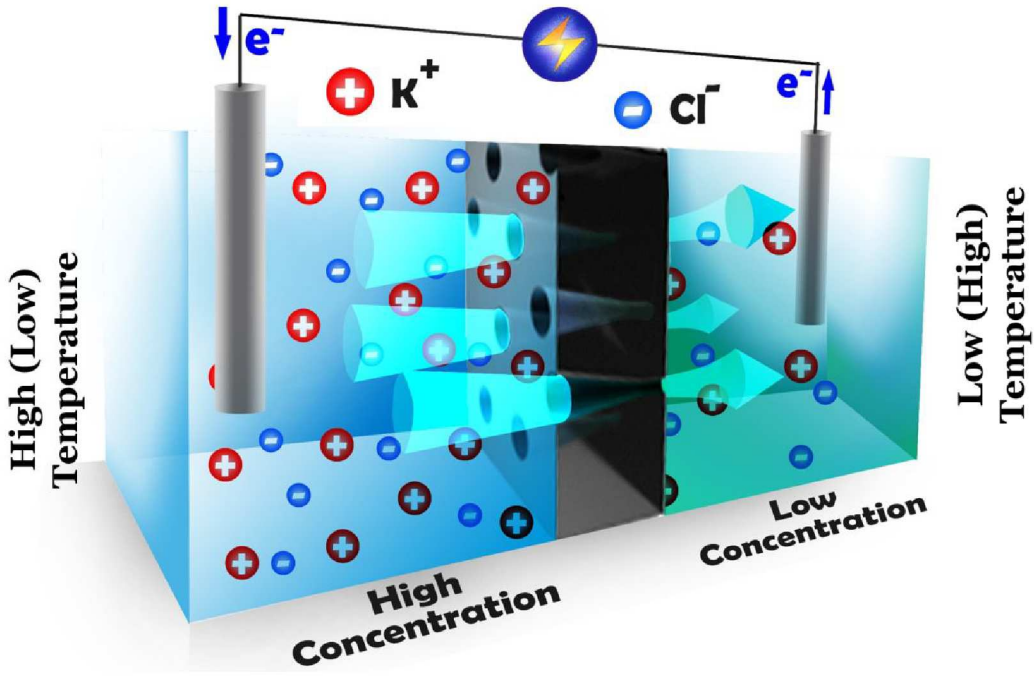

Fig. 1. The schematic of a funnel-shaped soft nanochannel subjected to the gradients of concentration and temperature. The interior/exterior walls of the channel are covered with a PEL.

2.1. Problem formulation

In order to arrive at Eqs. (1) to (5), which are the pertinent equations governing the underlying transport of the problem chosen in this analysis, the following assumptions are made: the system is at steady-state, flow sceneraio is in the creeping regime, and electrolyte is KCl solution, i.e. a Newtonian incompressible fluid. As a consequence of the non-isothermal flow conditions established in the nanochannel due to the applied temperature gradient, the physical properties of the electrolyte solution such as diffusivity, viscosity, permittivity, thermal conductivity, and density are affected by temperature and assumed to temperature-dependent as well. Several pertinent properties and their functional form with temperature are provided in Table 1. Meanwhile, several terms appearing in Eqs. (1)-(3) are dscirbed as follows. The electrolyte solution viscosity: μ, diffusion coefficient of ionic species in the electrolyte: D_j ($j = 1$ for cations (K^+), and $j = 2$ for anions (Cl^-)), the electrolyte permittivity: ε, the thermal

conductivity coefficient of the electrolyte: k, while p, $\mathbf{u}$, ϕ, $\mathbf{N}_j$, and T denote the hydrodynamic pressure, flow velocity, electric potential, flux of ionic species, and temperature, respectively. Accordingly, consistent with the asumptions taken here, the relevant equations, which are the Poisson-Nernst-Planck with thermal diffusivity, Stokes-Brinkman equation, and energy equation, take the following form as [16, 17, 62, 63, 69]:

$$\nabla^2\phi = -\frac{\rho_E + i\rho_{PEL}}{\varepsilon}, \qquad i = 0, 1 \tag{1}$$

$$\nabla . \mathbf{N}_j = \nabla . \left(c_j\mathbf{u} - D_j\nabla c_j - D_j S_T c_j \nabla T - D_j \frac{z_j F c_j}{RT}\nabla\phi \right) = 0 \tag{2}$$

$$\nabla \cdot \mathbf{u} = 0 \tag{3}$$

$$\mu\nabla^2\mathbf{u} - \nabla p - \rho_E\nabla\phi - i\gamma\mathbf{u} = 0\,, \qquad i = 0, 1 \tag{4}$$

$$\rho C_p \mathbf{u}.\nabla T + k\nabla^2 T = 0 \tag{5}$$

Note that the constant charge density of the soft layer is $\rho_{PEL} = eZ_{PEL}N_{PEL}$,where e, Z_{PEL} and N_{PEL} stands for the charge of electron, the valence, and the number density of the PEL fixed charged groups, respectively. The ionic density of the mobile ions in the electrolyte is defined as $\rho_E = \sum_{j=1}^{2} z_j F c_j$, where z_j and c_j are the charge numbers and concentrations of ionic species in the electrolyte, respectively. The Nernst Planck equation is corrected with the Soret effect and the term S_T appearing in Eq. (2) represents the Soret coefficient. It should be noted the Joule heating and the viscosity dissipataion effects, respectively, are the functions of the applied voltage. However, acounting for a minimal voltage in this case, impact these two effect is ignored in the analysis as witnessed in Eq. 5. Also, the term $\gamma = \lambda^2\mu_{PEL}$ in Eq. (4) represents

the friction coefficient, while terms F, R, C_p, ρ and T in aforementioned equations denote the Faraday constant, universal gas constant, specific heat capacity, fluid density, and the absolute temperature, repectively. A step function is defined as i being 0 and 1, outside and inside of the PEL, respectively [17, 69]. It is worth mentioning here that Eqs. (1)-(5) are solved considering a set of boundary conditions, whish are listed in Table 3 and shown in Fig. 2b as well [62, 63]. It should be noted that considering the creep flow regime in modified nanochannels with a soft layer, the effect of the convection term created by fluid motion and temperature gradient is insignificant. Therefore, according to Felderhoff's point of view, the created friction force cannot lead to the deformation of the soft layer. On the other hand, modifying the surface of the nanochannel into a soft layer leads to strengthening the electroosmotic flow.

Table 1: The properties of the physical system that change with temperature.

Parameter	Correlation	Description	Ref.
ε	$\varepsilon_0(a_1 + b_1T + c_1T^2)$	Relative permittivity of fluid	73
k	$a_2 + b_2T + c_2T^2 + d_2T^3$	Heat conductivity	73
ρ	$a_3 + b_3T + c_3T^2 + d_3T^3$	Fluid density	73
C_p	$a_4 + b_4T + c_4T^2 + d_4T^3 + e_4T^4$	Specific heat capacity	73
μ	$a_5\exp\left(\frac{b_5}{T} + c_5T + d_5T^2\right)$	Fluid viscosity	73
B	$a_6 + b_6T$	Electrolyte variable	74
D_{K^+}	$a_7(1 + b_7(T - 293.15))$	Diffusivity of K^+ in fluid	75
D_{Cl^-}	$a_8(1 + b_8(T - 293.15))$	Diffusivity of Cl^- in fluid	75
S_T	$a_9(1 - \exp((b_9 - T)/c_9))$	Soret coefficient	76

Table 2: The constant parameters listed in Table 1.

No.	a	b	c	d	e
1	2.51×10^2	-8.00×10^{-1}	7.38×10^{-4}	–	–
2	-8.70×10^{-1}	8.90×10^{-3}	-1.58×10^{-5}	7.98×10^{-9}	–

No.	a	b	c	d	e
3	8.39×10^{2}	0.14×10^{1}	-3.00×10^{-3}	3.72×10^{-7}	–
4	1.20×10^{4}	-8.04×10^{1}	3.10×10^{-1}	-5.38×10^{-4}	3.63×10^{-7}
5	1.86×10^{-14}	4.21×10^{3}	4.53×10^{-2}	-3.38×10^{-5}	–
6	1.91×10^{-1}	-5.648×10^{-4}	–	–	–
7	1.96×10^{-9}	2.50×10^{-2}	–	–	–
8	2.03×10^{-9}	2.50×10^{-2}	–	–	–
9	9.80×10^{-3}	2.93×10^{2}	1.02×10^{2}	–	–

Table 3: Boundary conditions considered for the computational regions illustrated in Fig. 2a.

Interfacial Surfaces	**Electrical potential (Eq. 1)**	**Ionic mass transfer (Eq. 2)**	**Flow Field (Eqs.3 and 4)**	**Heat Transfer (Eq. 5)**
$\boldsymbol{\Omega_1}$	electrically neutral $\mathbf{n}.\nabla\phi = 0$ or $\sigma_w = 0$	ion-impervious $\mathbf{n}.\mathbf{N}_j = 0$	non-slip $\mathbf{u} = 0$	insulation $\mathbf{n}.\nabla\mathbf{q} = 0$*
$\boldsymbol{\Omega_2}$	Continuous at the PE layer–liquid interface			
$\boldsymbol{\Omega_3}$	Grounded $\phi = 0$	bulk concentration $c_j = C_R$	no external pressure $p = 0$	Temperature $T = T_R$
$\boldsymbol{\Omega_4}$	constant voltage bias $\phi = V_{app}$	bulk concentration $c_j = C_L$	no external pressure $p = 0$	Temperature $T = T_L$
$\boldsymbol{\Omega_5}$	Insulation $\mathbf{n}.\nabla\phi = 0$	zero normal ionic flux $\mathbf{n}.\mathbf{N}_j = 0$	slip boundary	insulation $\mathbf{n}.\nabla\mathbf{q} = 0$

*** A note on q: it is equal to the heat flux.**

Simultaneous effects those stemming from the prevailing concentration and temperature gradients along side the applied voltage acorss the flow configuration drive the ions to move along the nanochannel. The undelrying ion transport phenomenon leads to the development of osmosis current, I_{os}, which is calculated as [16]:

$$I_{os} = \int F\left(\sum_{j=1}^{2} z_j \mathbf{N}_j\right) \cdot \mathbf{n}\mathrm{dA} \qquad (6)$$

Where, A reperesents the cross sectional area of either reservoir.

Assuming that I_+ and I_- are the osmotic currents associated with K^+ and Cl^- ions, respectively, the transference number, t_+, is given as [17]:

$$t_+ = \frac{I_+}{I_+ + |I_-|} \tag{7}$$

According to its definition, t_+ varies between 0 and 1. The channel is anion-selective if $0 < t_+ < 0.5$, and becomes cation-selective for $0.5 < t_+ < 1$. It is worth to add here that, for $t_+ = 0.5$, the channel does not show ion-selectivity [69].

Again by referring to Fig. 2b, effort is taken here to determine the efficiency of salinity energy generation. The salinity energy generation would result in E_{diff}, R_{pore}, and R_{load}, signifying the diffusion potentials, the inner resistance of channel, and the resistance of the electrical load, respectively. Based on the terminology provided in Fig. 2b, the electric potential created in the nanochannel, V_{pore}, is calculated as [62, 63]:

$$V_{pore} = E_{diff} - IR_{pore} = IR_{load} \tag{8}$$

Now, the salinity energy generated in the nanochannel, P_{pore}, can be written as:

$$P_{pore} = IV_{pore} \tag{9}$$

By using Eqs. (8) and (9), the expression for the generated salinity energy yields as:

$$P_{pore} = E_{diff}^2 \frac{R_{load}}{(R_{load} + R_{pore})^2} \tag{10}$$

The efficiency of salinity energy generation η, is defined as the ratio of the electrical power retrieved from the nanochannel to the Gibbs free energy of mixing, and it mathematical expression takes the following form [77]:

$$\eta = \frac{IV_{pore}}{(\mathbf{N}_+ + \mathbf{N}_-)RT\ln\left(\frac{\gamma_H C_H}{\gamma_L C_L}\right)} \tag{11}$$

In Eq. (11), $\mathbf{N}_+$ ($\mathbf{N}_-$) represents the flux of cations (anions), and γ_H (γ_L) denotes the activity coefficient of the electrolyte when the ionic concentration is high (low), C_H (C_L), respectively. The activity coefficient of a strong electrolyte is given by following equation as [74]:

$$\log \gamma_{H(L)} = \frac{-0.511\sqrt{I_s}}{1+\sqrt{I_s}} + \frac{(0.06+0.6B)I_s}{(1+1.5I_s)^2} + BI_s \tag{12}$$

Note that in Eq. (12) $I_S = \frac{1}{2}\sum_{i=1}^{2} c_i z_i^2$ denotes the ionic strength, and B refers to the electrolyte variable for KCL, as provided in Table 1.

Neglecting the non-linear influences, the maximum salinity energy P_{max}, is generated when $V_{pore} = E_{diff}/2$ and $R_{pore} = R_{load}$. The maximum salinity energy reads as:

$$P_{max} = \frac{E_{diff}^2}{4R_{pore}} \tag{13}$$

Considering $V_{pore} = E_{diff}/2$ and $\mathbf{N}_+/\mathbf{N}_- \cong t_+/(1-t_+)$, and recalling Eq. (12), the efficiency corresponding to the maximum of generated salinity energy becomes:

$$\eta_{max} = \frac{(2t_+ - 1)\left(\frac{E_{diff}}{2}\right)}{\frac{RT}{z_i F}\ln\left(\frac{\gamma_H C_H}{\gamma_L C_L}\right)} \tag{14}$$

All of the variables in Eq. (14) are expressed in terms of the main physicochemical properties of the problem except for E_{diff}, which is described by the following expression [78]:

$$E_{diff} = (2t_+ - 1)\frac{RT}{z_i F}\ln\left(\frac{\gamma_H C_H}{\gamma_L C_L}\right) \quad (15)$$

Substituting the expression of E_{diff}, as in Eq. (15), in Eq. (14), the formula of η_{max} is simplified as:

$$\eta_{max} = 0.5(2t_+ - 1)^2 \quad (16)$$

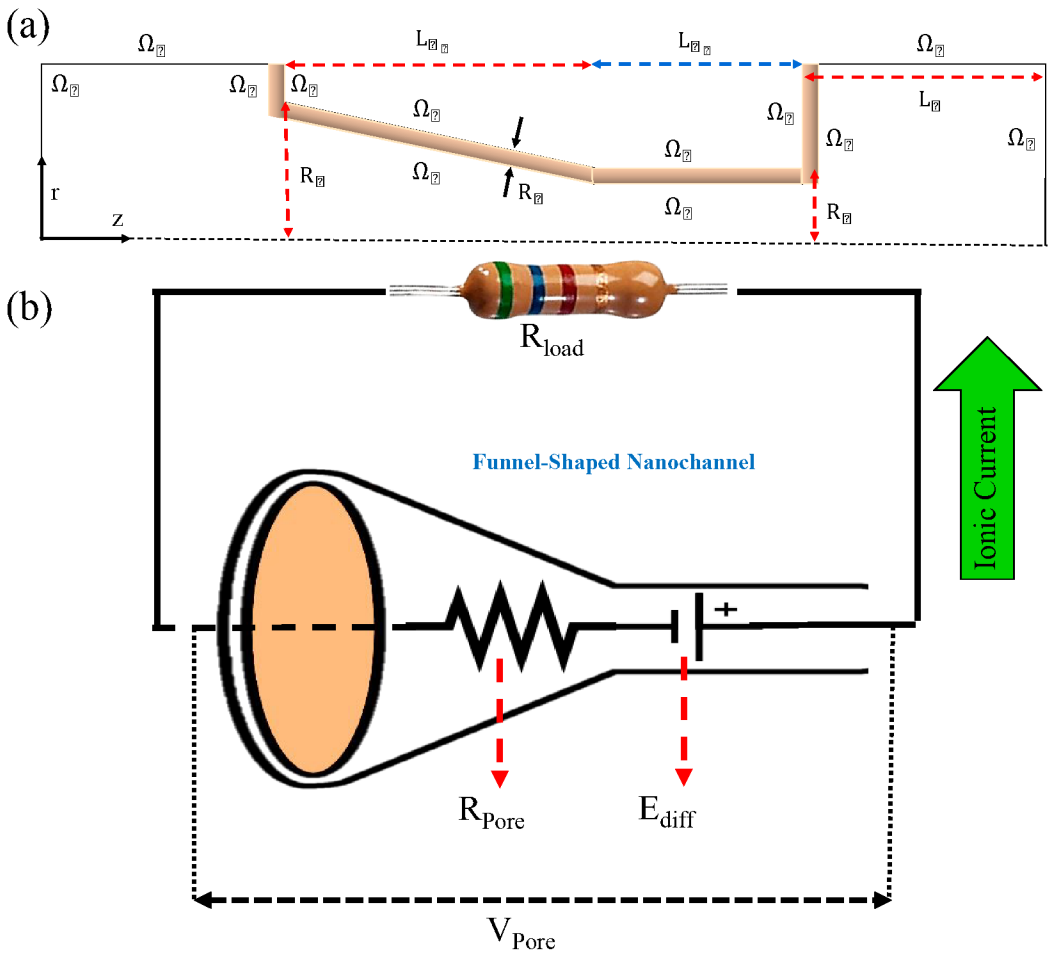

Fig. 2. (a) 2-D view of the soft nanochannel including the reservoirs, the coordinate system with the PEL, and schematic of a funnel-shaped nanochannel with the boundary conditions applied in simulation, (b) a simple equivalent electrical circuit of the reverse electrodialysis process. The nanochannel, which connects two identical large reservoirs filled with aqueous KCl solutions, has length of the conical section L_{N1}, the cylindrical section L_{N2}, the tip radius R_T and the base radius R_B. (Please note that Ω_i exhibits interfacial surfaces).

2.2. Solution approach

Given that Eqs. (1) to (5) are interdependent and highly nonlinear; the solution of these transport equations implores a relevant appraco consistent with numerical method. In this analysis, equations are solved by using the finite element framework of Comsol Multiphysics®. In order to simulate the present problem in a combination of triangular and square meshes is employed. The grid performance study of the chosen configuration is also conducted only to determine the optimal mesh count. The results, as shown through the depiction of .. in Fig. (xx), revealed that 40,000 meshes are sufficient to obtain the desired results without compromising the desirted flow physics. Nonetheless, it may be mentione here that extremely fine meshes are applied near the PEL to accurately capture the electric double layer (EDL) phenomenon. The direct MUMPS solver with a maximum relative tolerance of 10^{-8} is used for all the simulations [62, 63].

3. Results and discussions

This study primarilly focuses on how the temperature and concentration gradients affect the osmotic current and electroosmotic flow in a funnel-shaped nanochannel with built-in a dense PEL at its inner wall surface. Interestingly, as seen from the present analysis, the temperature and concentration ratios are found to be very vital to alter the underlying ionic transport in the chosen configuration. The numerical values of several model parameters used in the simulation are provided in Table 4.

Table 4: Physicochemical parameters considered in simulations.

Parameter	Description	Value
C_R	Right tank bulk concentration	1 mM
C_L	Left tank bulk concentration	$10 - 1000$ mM
T_R	Right tank temperature	$10 - 80$ °C

Parameter	Description	Value
T_L	Left tank temperature	$10-80$ °C
N_{PEL}/N_A	Density of PEL fixed charges divided by Avogadro's number	$100\ mol/m^3$
Z_{PEL}	Valance fixed charge ions in soft layer	-1
L_R	Length of cylindrical reservoirs	200 nm
L_{N_1}	Length of conical Nanochannel section	500 nm
L_{N_2}	Length of cylindrical Nanochannel section	500 nm
R_B	Bottom Radius	100 nm
R_T	Top Radius	20 nm
R_S	PEL Thickness	10 nm
r_A	Ionic Radius of Cl^-	3.3×10^{-10} m
r_c	Ionic Radius of K^+	3.3×10^{-10} m
T_{ref}	Reference temperature	298.15 K
k_B	Boltzmann constant	1.38×10^{-23} J/K
ε_0	Permittivity of vacuum	8.854×10^{-12} F/m
e	Elementary charge	1.6022×10^{-19}C
F	Faraday constant	96500 C/mol
R	Gas constant	8.3145 J/(mol.K)
λ	Friction factor	1×10^9
$\lambda_C=\frac{C_L}{C_R}$	Concentration ratio	$10-1000$
$\lambda_T=\frac{T_L}{T_R}$	Temperature ratio	$1-8$

The nanochannels can demonstrate selectivity depending on the sign of the charge of PEL. Throughout the present study, the charge of the PEL is considered as negative, which makes the nanochannels selective towards the cations, i.e. K^+ ions [17].

We begin our discussion with the plot showing the current-potential-power curves of funnel-shaped soft nanochannel as illustrated in Fig. 3. As can be seen in Fig. 3, the variations for both

modes of type I and type II have been depicted by considering various temperature ratios (λ_T), and concentration ratios (λ_C). The ohmic behavior of nanochannels towards the conducting current is shown by the linear decrease of the ionic current with an electrical voltage increment. The ohmic behavior of the nanochannel implies that the electric voltage has no major effect on the concentration of ionic species. The SEG generates small electric fields in the nanochannels, which do not cause ionic concentration polarization. Thus, regardless of the direction of the gradient, the greater is the concentration and/or temperature ratios, the greater is the ionic current as witnessed in Fig. 3. Due to the ion-selective nature of the nanochannels, the zero current-voltage and zero voltage-current curves are evident from the changes in the diffusion fluxes of cations and anions on the $\mathrm{I}-\mathrm{V}$ curves [62]. This voltage and current are referred to as E_{diff} and I_{OS}, respectively. As defined earlier, the maximum salinity energy is generated when $V_{pore} = E_{diff}/2$, while one can use Eq. (13) to estimate this quantity. As can be seen in Figs. 3(a) and (b), for the funnel-shaped nanochannel for both modes of type I and type II, the transference number t_+, increases with decreasing the value of concentration ratio λ_C. This observation is attributed to the overlapping phenomenon of electrical double layers which are significantly developed on the nanochannel walls. On the other hand, t_+ is seen to be higher in the counter-current mode [43].

The slope of the straight lines in Figs. 3(a) and (b), i.e., R_{pore}, which shows the $\mathrm{I}-\mathrm{V}$ curves, is obtained based on Eq. (8) and seems to inversely proportional to electrical conductance. As expected, the electrical conductivity increases with increasing the value of concentration ratios. At different concentration ratios λ_C, a variance in the ionic selectivity behavior is apparent, and brings about a variation in the slope of electrical conductance. As shown in Figs. 3(a) and (b), for higher λ_C, a higher electrical conductance is obtained, resulting

in a smaller slope, which in turn reveals a higher current transmission occurs in the nanochannel. Furthermore, the ionic current is greater (less) in counter-current (co-current) mode since where the gradients of concentration and temperature are in the same (opposite) direction, the nanochannel acts as an amplifier (attenuator). At high concentration ratios, it is remarkable to note the significant contribution of the diffusion that makes to the total ionic flux to be larger than the migration of ions. The maximum salinity energy generation is also increased with increasing the value of λ_C at counter-current mode, thus providing higher salinity energy generation than the co-current mode; since the transference number for type II is greater than that for type I. Additionally, it is clear from Eqs. (13) and (15) that since diffusion potential is a strong function of transference number, and P_{max} is directly related to diffusion potential, the maximum generation of salinity energy in the counter-current mode (type II) will be greater than that in the co-current mode (type I).

Figures 3(c)-(d) show how increasing the value of temperature ratio increases both co-current and counter-current ionic currents at a particular concentration ratio. Because of the rising temperature, the Soret effect becomes more significant, which in turn, leads to an enhancement of the ionic current in the process. As shown in Fig. 3(c), in the type I mode of operation, the transference number decreases with increasing the temperature ratio, thus according to Eq. (15), the diffusion potential also decreases. In line with the similar argument, this trend is reversed in type II. As such, following this analogy, the salinity energy generated in type II becomes significantly higher than that generated in type I [69].

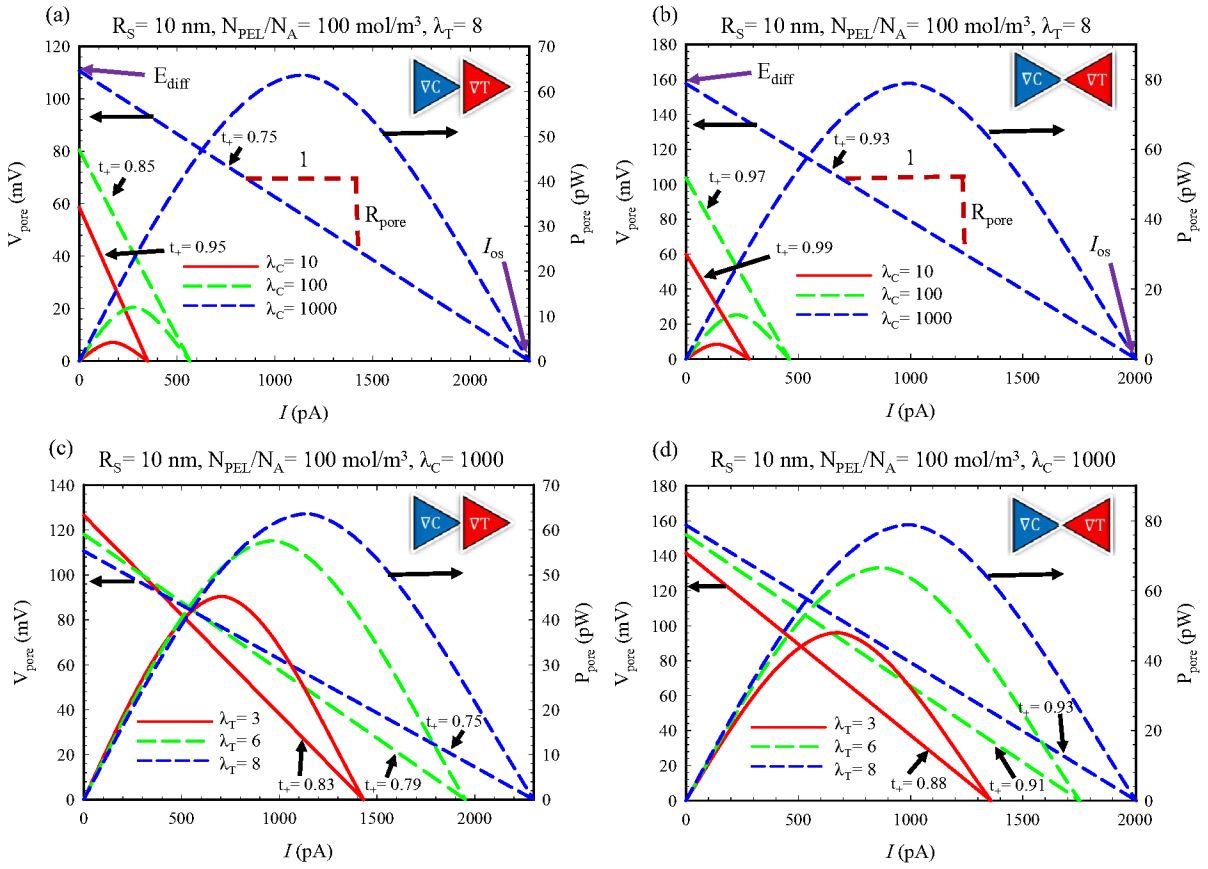

Fig. 3. The current-voltage-power graphs at different concentration- and temperature ratios considering (a),(c) type I and (b),(d) type II.

Figure 4 illustrates the variation of osmotic current I_{OS} versus concentration and temperature ratios, obtained for both co-current and counter-current modes. It is observed in Fig. 4(a) that I_{OS} increases with increasing the value of λ_C for both co-current and counter-current modes. This variation is as expected because the ions in nanofluidic channels are more significant for a higher bulk concentration (note that C_R is fixed). It should be pointed out from the depicted variation in Fig. 4(a) that, the increasing dependence of I_{OS} on λ_C is observed irrespective of which tank possesses the higher ionic concentration. As shown in Fig. 4a, I_{OS} is higher in the co-current mode than in the counter-current mode. The underlying physical reasoning behind

this observation is as follows: in this state, the driving forces due to concentration and temperature gradients are in the same direction, thus amplifying the ionic current in the process. Figure 4(b) demonstrates the osmotic current in the funnel-shaped nanochannel obtained for different temperature ratios for both co-current and counter-current modes. With an increase in λ_T, the osmotic current increases as seen from Fig. 4(b), and this observation is attributed to the consequential effect of augmented Soret efect on the underlying transport. Therefore, by increasing S_T (i.e., the mass flux created by a temperature gradient), the mobility of ions increases; thus, the ionic current is amplified. In line with the observation as in Fig. 4(a), the ionic current of the co-current mode is seen to be higher than the counter-current mode in this present analysis [75].

Figures 5(a)-(b) present contour plot of the osmotic current as the function of concentration and temperature ratios. As mentioned earlier, regardless of which tank has a higher temperature or concentration, the osmotic current increases with increasing the magnitude of temperature and concentration gradients. We have attributed this observation to the giant enhancement of the number and mobility of ionic species. Additionally, it is observed from Figs. 5(a)-(b) that in the co-current mode, the similarity in the direction of both gradients have positive effect on the osmotic current, and consequently, on its development in the underlying phenomenon. On the other hand, in the counter-current mode, the prevailing trend reduces the osmotic current as compared to co-current mode due to the presence of resistance of driving forces against each other [63].

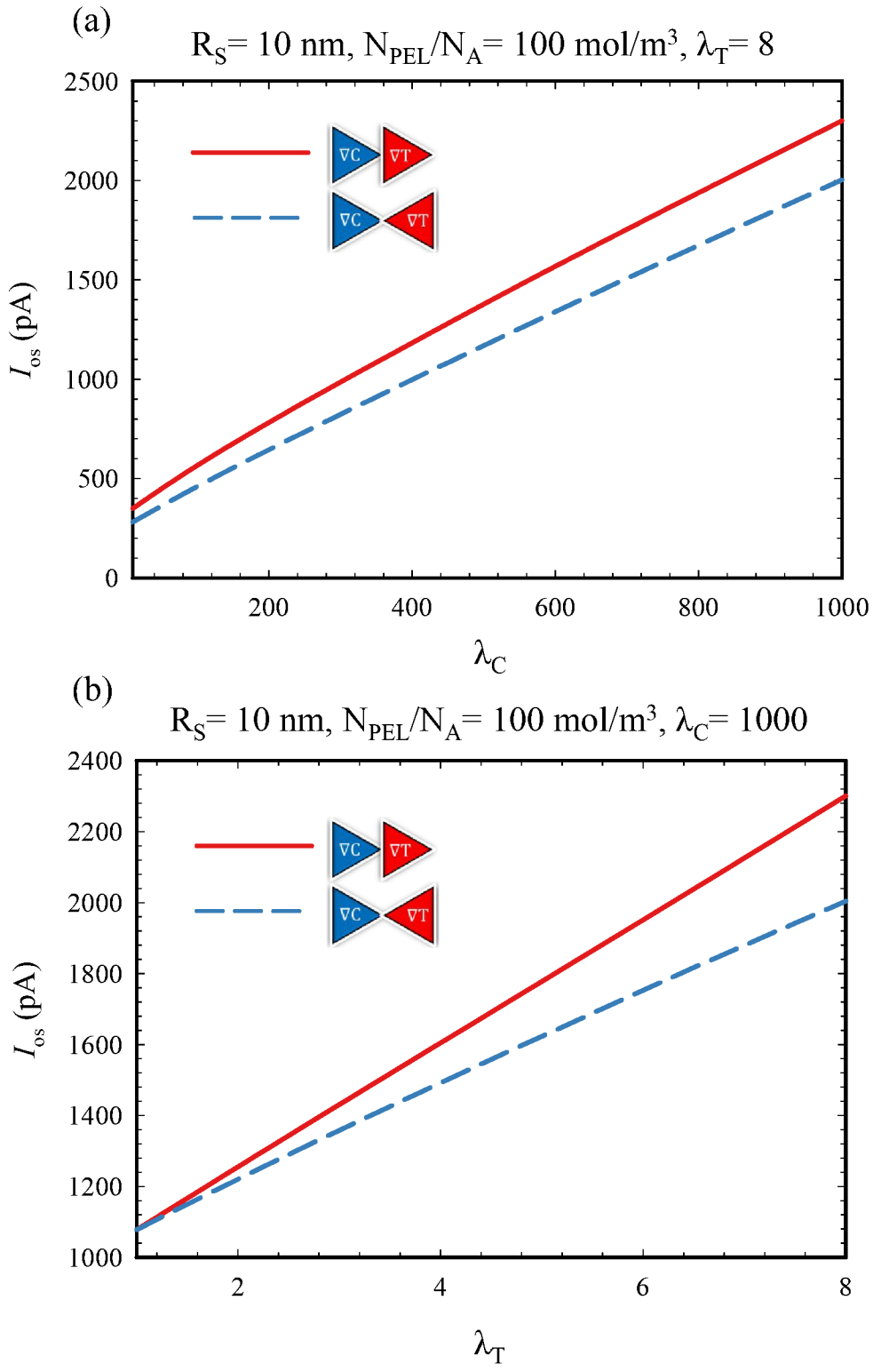

Fig. 4. The osmotic current I_{OS}, for both modes of co-current and counter-current vs. (a) concentration ratio, (b) temperature ratio.

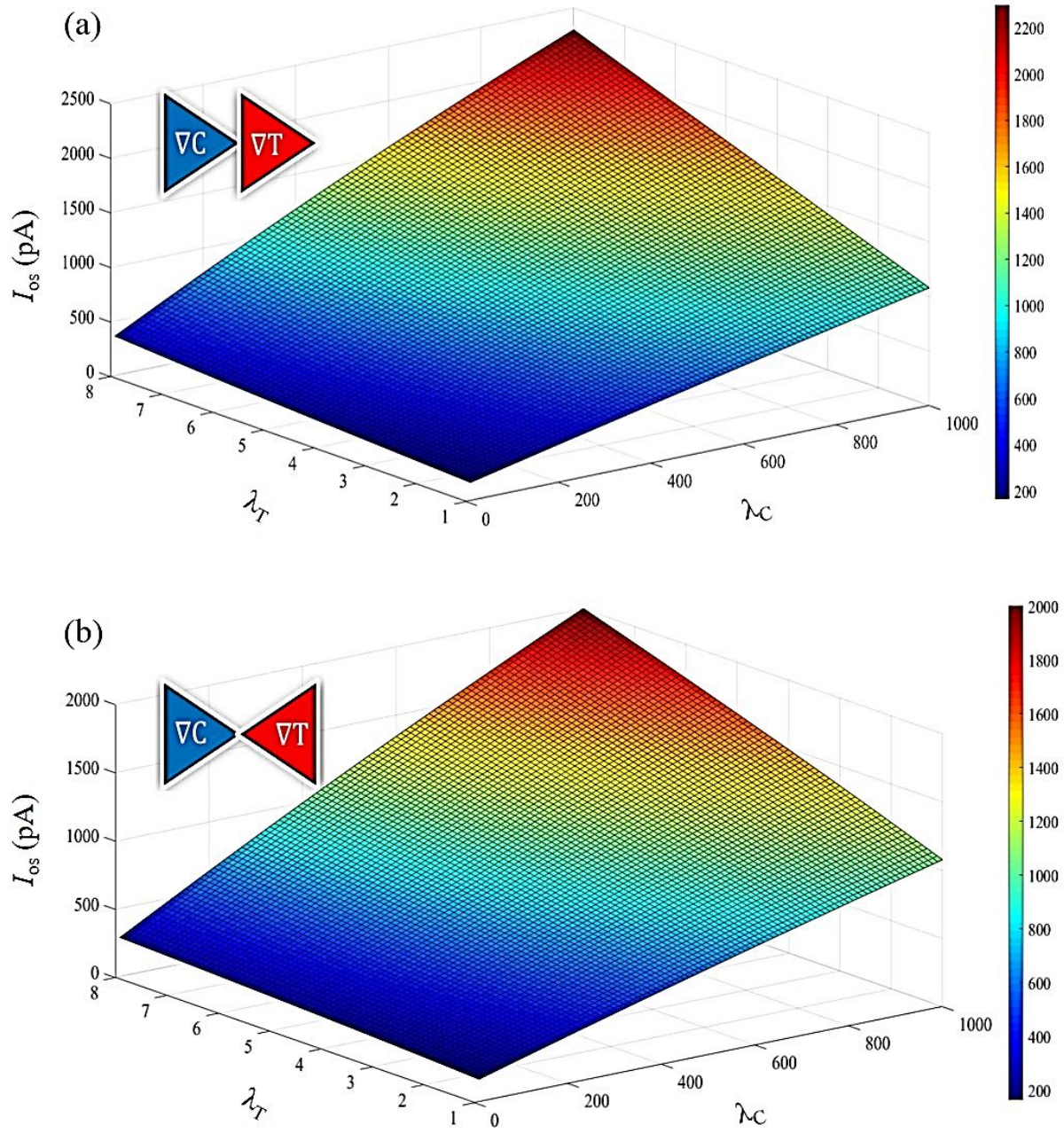

Fig. 5. The impacts of concentration and temperature ratios on osmotic current I_{OS}, for (a) co-current mode, and (b) counter-current mode.

Figure 6 plots the dependence of the transference number t_+ (Figs. 6a,b), and the diffusion potential E_{diff} (Figs. 6c, d), on the ionic concentration and temperature ratios for both co-current and counter-current modes. Note that Fig. 6(a) reconfirms our previous result that a decrease in the transference number is accompanied with an increase in the concentration ratio for both co-current and counter-current modes. The transference number, irrespective of the directions of the temperature and concentration gradients, decreases with increasing the value of concentration ratio at a constant temperature ratio. According to Eq. (7), the concentration ratio is adversely proportional to transference number because an increase in the bulk cocentration dampens out the EDL overlapping phenomenon to the extent possible. Therefore, while the flux of the cations is more significant than that of the anions for the smaller concentrations, the ionic fluxes get closer to higher bulk concentrations, and results in a reduction in the transference number. The EDL being formed occupies only a small fraction of the nanochannel cross-sectional area when the concentration ratio is very large [16]. Hence, it is because of this reason, the transference number reveals a weaker dependence on the concentration ratio. Important to mention, under these conditions, the number of ions in the channel becomes so large that, despite the lower strength of the external electric field applied along the channel, a considerable amount of electroosmotic flow occurs in the fluidic pathway. In addition, as shown in Figs. 4(a)-(b), the osmotic current becomes higher in the co-current mode than in the counter-current mode. So, in this state, more ionic species will pass through the nanochannel, which in turn, will lead to a further reduction in the transference number.

Fig. 6(b) shows the transference number t_+, in terms of temperature ratio, obtained at constant concentration ratio for both co-cuurent and counter-current modes. As shown in Fig. 6(b), in the counter-current mode, the high temperature becomes closer to the selective section

of the channel, and the counterions are seen to be more mobile than the coions. These effects give rise to an increase in the transference number as witnessed in Fig. 6(b). On the other hand, in line with our observation and the discussion pertaining to Fig. 3, in the co-current mode as seen in Fig. 6(b), the trend is reversed [63].

Figure 6(c) confirms that an increase in either of the concentration and temperature ratios is accompanied by an increase in the diffusion potential for both co-current and counter-current modes. This is not unusual because the driving force of ion diffusion transport, i.e., the concentration and temperature gradients, increases with increasing the magnitude of λ_C and λ_T. In other words, with an increase in the concentration and temperature ratios, the number of ions as well as mobility of ions increases; thus, the diffusion potential gets strengthened. In addition, Fig. 6(d) shows the variation of the diffusion potential versus the temperature ratio at constant concentration ratio for both co-current and counter-current modes. As seen from the depicted variation in Fig. 6(d) and can be verified from Eq. (8) as well, the diffusion potential is found to be a powerful function of the transference number. Also, in line with the reported observation[17, 69], the diffusion potential in the counter-current mode is seen to be more significant than that in the co-current mode peratining to the present analysis as well.

Fig. 7 represents 3D contour for transference number and diffusion potential, mapped in the plane of concentration and temperature ratios, for co-current and counter-current modes. As mentioned in all panels of Fig. 7, for both co-current and counter-current modes, by increasing the concentration ratio, the transference number (diffusion potential) is decreased (increased). Also, at co-current (counter-current) mode, by increasing the temperature ratio, the transference number (diffusion potential) is decreased (increased).

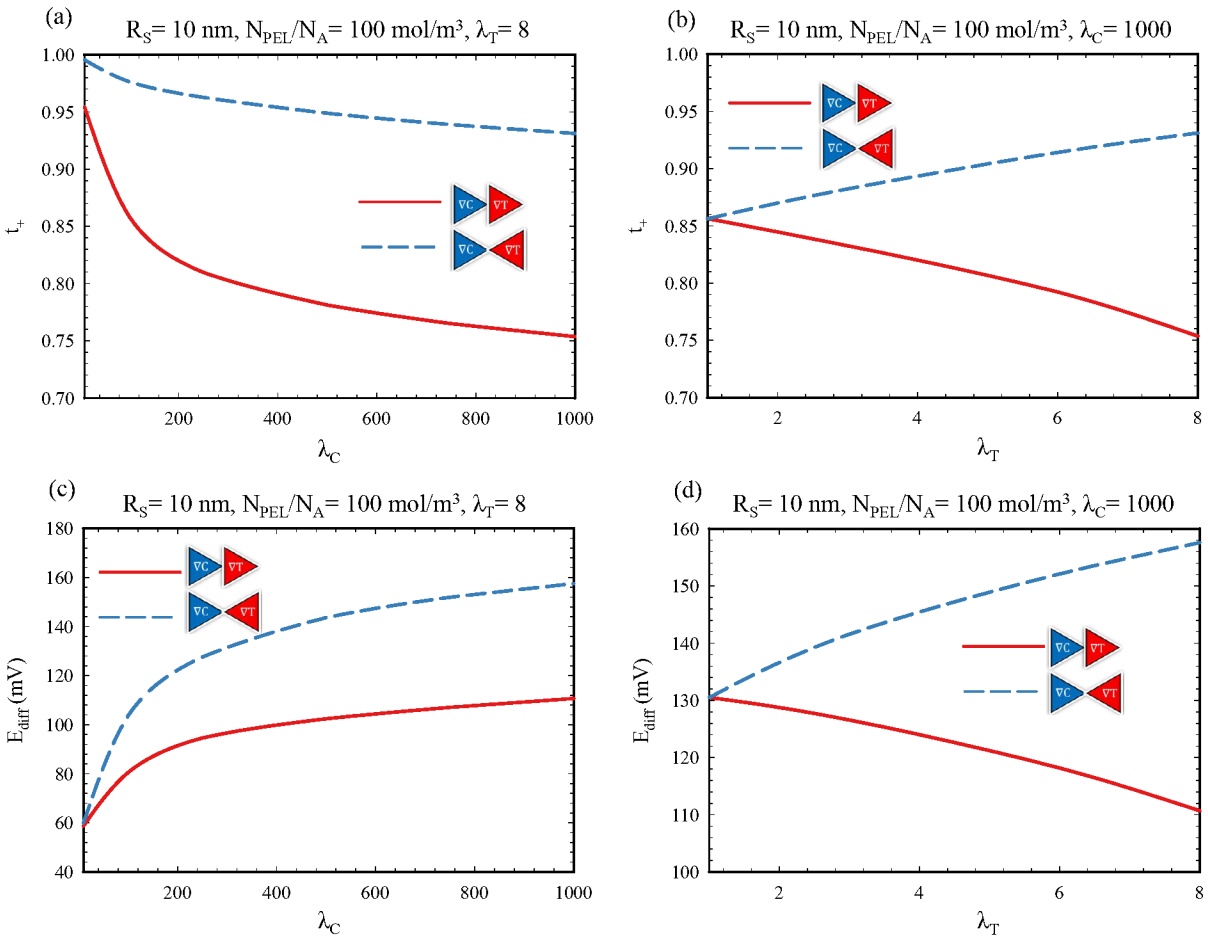

Fig. 6. The transference number, t_+, and diffusion potential, E_{diff}, for both co-current and counter-current modes vs. (a),(c) concentration ratio, and (b),(d) temperature ratio.

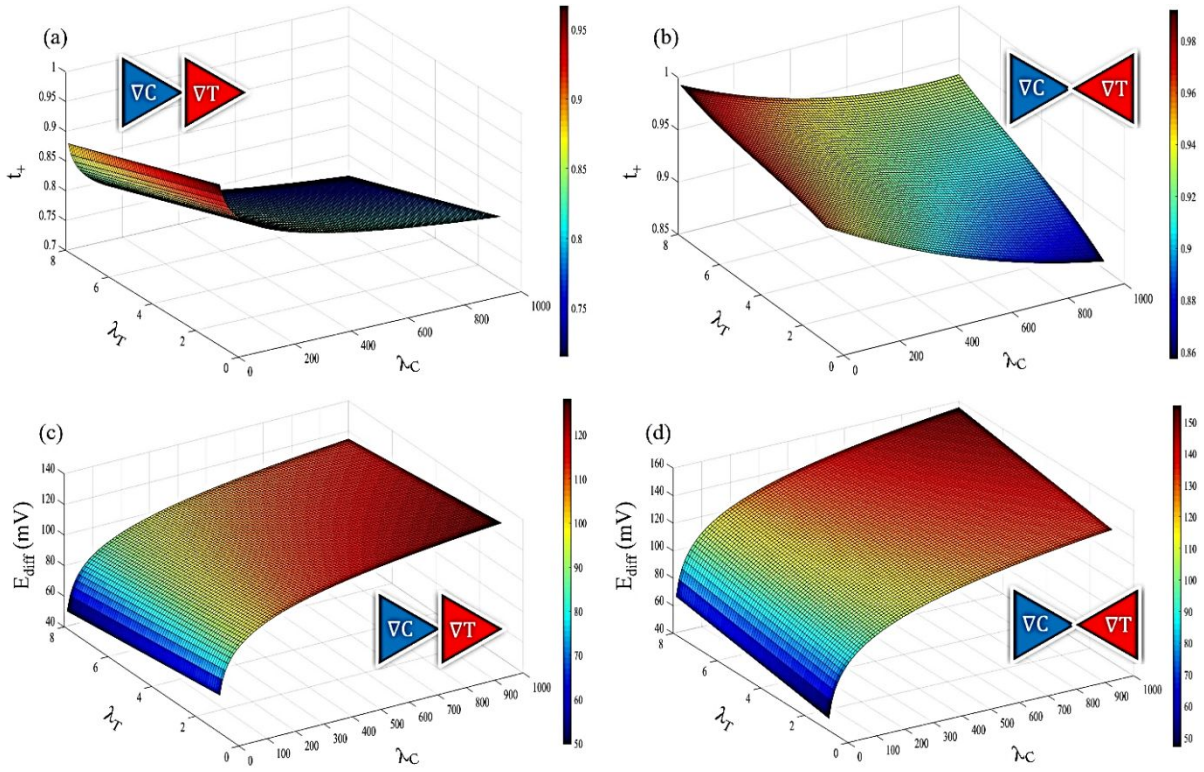

Fig. 7. The impacts of concentration and temperature ratios on the transference number, t_+, and the diffusion potential, E_{diff}, for (a),(c) co-current mode, and (b),(d) counter-current mode.

The impact of the concentration and temperature ratios on the maximum value of generated salinity energy (P_{max}), and the maximum efficiency of salinity energy generation (η_{max}), at both co-current and counter-current modes is illustrated in Fig. 8. As shown in Fig. 8(a), and simultaneusly verified by Eq. (14), η_{max} decreases with increasing the value of concentration ratio for both cases of co-current and counter-current modes, while it increases with increasing the magnitude of diffusion potential and the transference number. Meanwhile, in sharp contrast to the transference number, the diffusion potential being an increasing function of the concentration ratio, the overall dependence of the maximum efficiency of salinity energy generation on the concentration ratio relies on the interaction between the effects of transference number and concentration ratio from one side and diffusion potential from the other side. As mentioned earlier, in the co-current mode, both the transference number and the

diffusion potential have a decreasing trend. It is because of this reason the overlapping effect of these two parameters on the efficiency of salinity energy generated as evident in Eq. (14), directly reduces the η_{max}. However, in the counter-current mode, the transference number decreases, and the diffusion potential increases. The combined effects of these two factors in the counter-current mode eventually lead to a decrease in η_{max} at a lower rate. Moreover, as seen in Fig. 8b, for co-current (counter-current) mode, η_{max} decreases (increase) with increasing the temperature ratio, and this trend shows similarity with the reported observation [62, 63].

As observed in Figs. 8(c) and (d), in both co-current and counter-current modes, the maximum salinity energy generation increases with increasing the value of concentration and temperature ratios. The underlying physical reasoning behind this observation is as follows. In counter-current mode, by increasing the concentration and temperature ratios, the value of the physical parameters controlling the maximum salinity energy generation (P_{max}), i.e., the diffusion potential and the osmotic current increases, leading to the enhancement of P_{max}. Nevertheless, in co-current mode, albeit an increase in the concentration and temperature ratios enhances the osmotic current, an increase (decrease) in diffusion potential is the consequential effect due to increasing the magnitude of concentration (temperature) ratio. Note that the maximum value of salinity energy generation for counter-current mode is more than that obtained in co-current mode.

Fig. 9 illustrates 3D contour of the maximum generated salinity energy (P_{max}), and the maximum efficiency of salinity energy generation (η_{max}), in the plane of concentration and temperature ratios, plotted for both co-current and counter-current modes. As shown in Fig. 9(a), for co-current mode, with increasing the magnitude of concentration and temperature ratios, the maximum efficiency of salinity energy generation gets decreased. Also, as witnessed

in Fig. 9(b), at counter-current mode, with increasing the magnbitude of concentration (temperature) ratio, the maximum efficiency of salinity energy generation is decreased (increased).

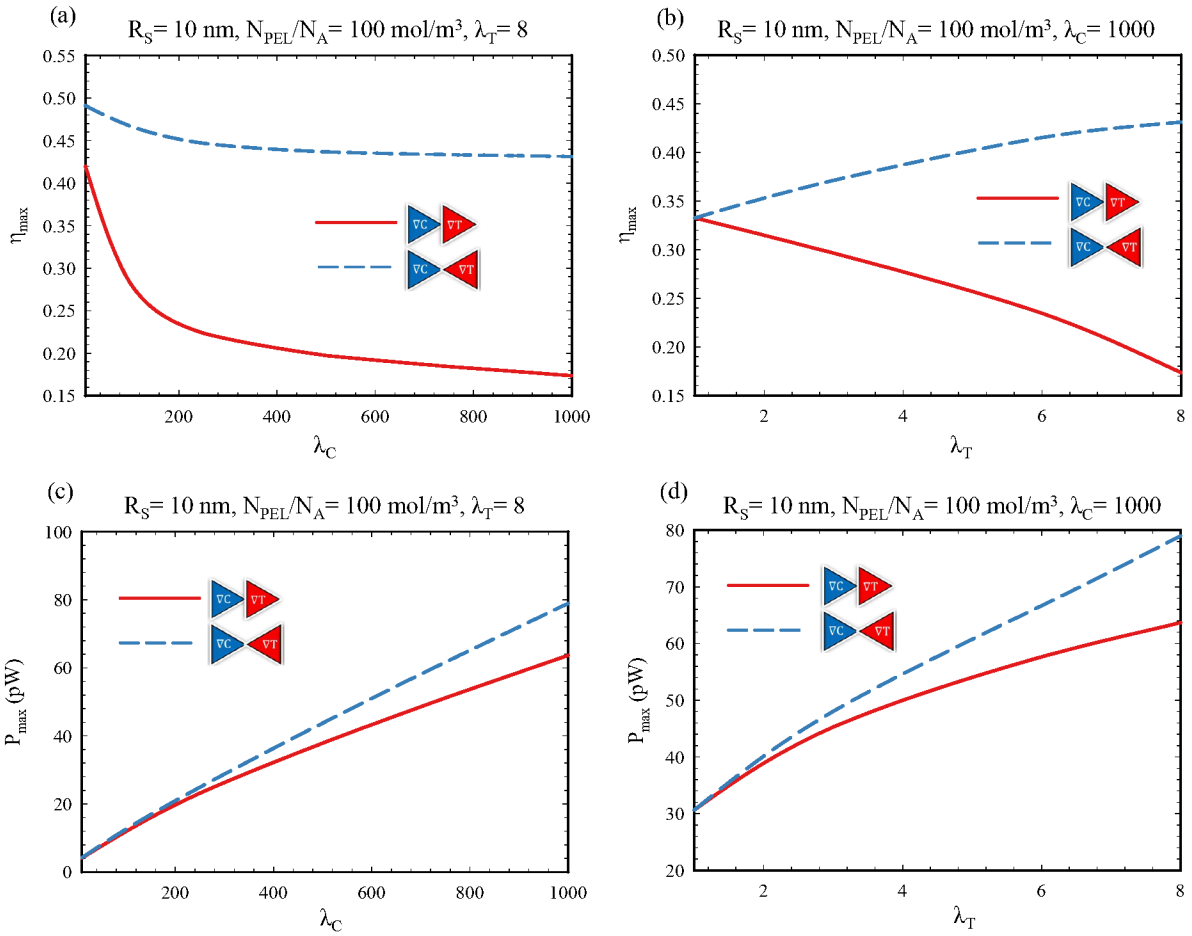

Fig. 8. The maximum efficiency of salinity energy generation, η_{max}, and the maximum generated salinity energy, P_{max}, for both co-current and counter-current modes vs. (a),(c) concentration ratio, and (b),(d) temperature ratio.

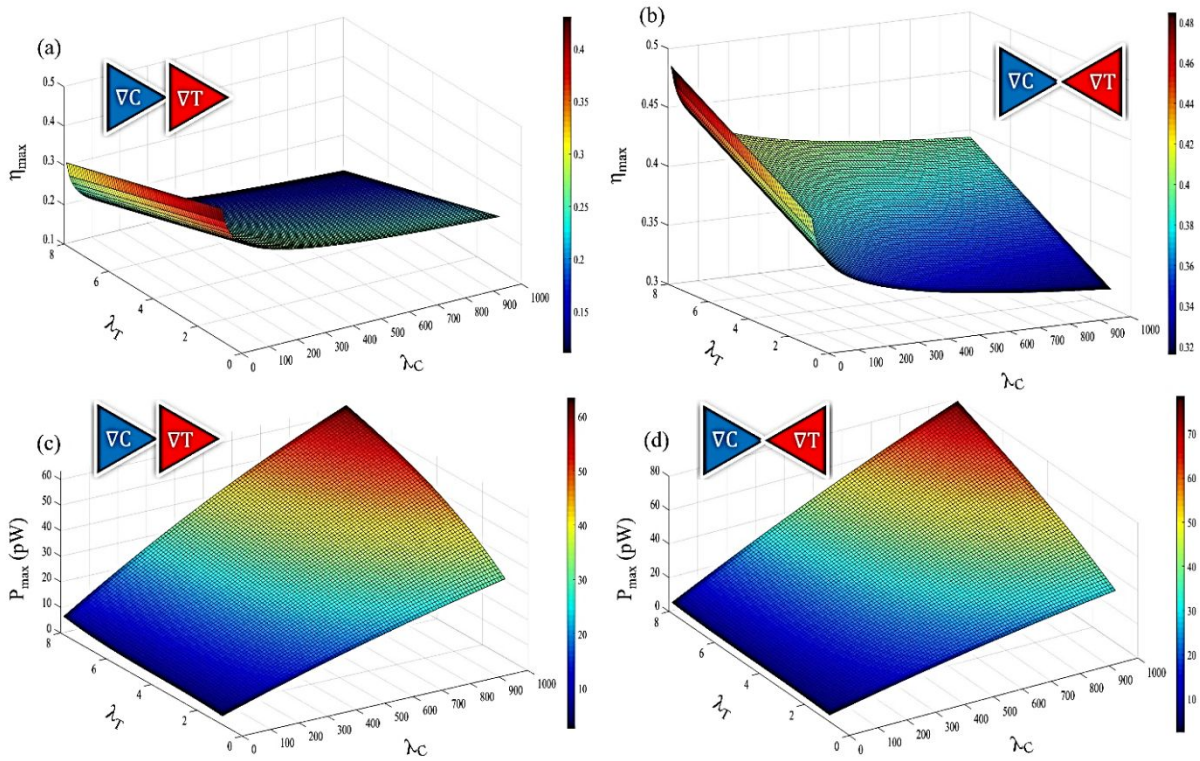

Fig. 9. The impacts of concentration and temperature ratios on the maximum efficiency of salinity energy generation, η_{max}, and the maximum generated salinity energy, P_{max}, for (a),(c) co-current mode, and (b),(d) counter-current mode.

Finally, for better comparison, performance of the simulated soft funnel-shaped nanochannel (current work) and other nanochannel geometries with different conditions (some recent works) were compared as summarized in Table 5. As can be observed, the soft funnel-shaped nanochannel simulated in this work shows a desirable power density. This work shows that the considering temperature-dependent properties and also the temperature gradient as a driven force can be used to improve power generation and performance of the maximum efficiency of salinity energy generation, effectively.

Table 5: Comparison of the nanochannels-based blue energy generation performance.

Ref.	Geometry	Type of nanochannel wall	Concentration gradient	Temperature gradient	Power density (W/m^2)
Hsu et al. [79]	Conical	Solid-state	Applied	--	18.2
Kang et al. [22]	Cylindrical	Solid-state	Applied	--	9.9
Khatibi et al. [62]	Conical	Soft-state	Applied	--	51.5
Kim et al. [44]	Cylindrical	Solid-state	Applied	--	7.7
Khatibi et al. [63]	Conical	Soft-state	Applied	--	75
Li et al. [80]	Cylindrical	Solid-state	Applied	Applied	72
This work	Funnel	Soft-state	Applied	Applied	101

4. Conclusions

The system under consideration consists of a funnel-shaped soft nanochannel connecting two cylindrical large reservoirs, filled with KCl electrolyte solution. First, the osmotic current, transference number, diffusion potential, maximum efficiency of salinity energy generation, and maximum generated salinity energy in the nanochannel were numerically investigated for varying temperature and concentration ratios. Next, the Poisson and modified Nernst-Planck, Navier-Stokes (Stokes-Brinkman), and energy equations were simultaneously solved using the finite element method, and the simulated results were analyzed systemtaically. For the present endeavour, results were obntained for both co-current and counter-current modes. Then, using the osmotic currents which pass through the nanochannel, their current-voltage-power response was examined. The main conclusions of the present analysis, which report the I_{os}, t_+, E_{diff}, η_{max}, and P_{max} behaviors of the funnel-shaped soft nanochannel, are summarized as follows:

1) It was shown that the osmotic current and the maximum generated salinity energy are both increasing functions of the concentration and temperature ratios for both co-current and

counter-current modes. In contrast, the dependence of the transference number, the diffusion potential, and the maximum efficiency of salinity energy generation on the concentration and temperature ratios are generally non-monotonic.

2) Irrespective of the directions of temperature and concentration gradients, the osmotic current increases with increasing the concentration and temperature ratios and seen to be always higher in the co-current mode.
3) The transference number at a constant temperature ratio continuously decreases with increasing the concentration ratio for both co-current and counter-current modes. However, the transference number at a constant concentration ratio decreases with increasing the temperature ratio in co-current mode and increases in counter-current mode.
4) The diffusion potential at a constant temperature ratio continuously increases with increasing the concentration ratio for both co-current and counter-current modes. Nevertheless, the diffusion potential at a constant concentration ratio decreases with increasing the temperature ratio in co-current mode and increases in counter-current mode.
5) The maximum efficiency of salinity energy generation at a constant temperature ratio continuously increases with increasing the concentration ratio for both co-current and counter-current modes. However, the maximum efficiency of salinity energy generation at a constant concentration ratio decreases with increasing the temperature ratio in co-current mode and increases in counter-current mode.
6) Regardless of the directions of the temperature and concentration gradients, the maximum generated salinity energy increases with increasing the concentration and temperature ratios and found to be always higher in the counter-current mode.

7) When nanofluidic channels, or membranes, are placed between electrolyte solutions of different temperatures, a large amount of energy conversion results in from low-grade heat sources (<100 °C).
8) The thermo-osmotic energy conversion can also be enhanced by combining thermal and concentration gradients. The ionic thermal up-diffusion significantly improves the membrane potential and ion selectivity for a case when temperature gradient acts in the opposite direction of the concentration gradient in the fluidic configuration. Pertaing to case of counter-current mode, with a constant concentration ratio (1000), increasing the magnitude of temperature ratio from 1 to 8 results in an increase in salinity energy from 30 pW to 80 pW.

Acknowledgments

The research council at Iran University of Science and Technology (IUST) is highly appreciated for its financial support during the course of this research.

CRediT authorship contribution statement

Mohammad Karimzadeh: Methodology, Software handling, Validation, Writing - original draft. **Mahdi Khatibi**: Conceptualization, Methodology, Writing - review & editing. **Seyed Nezameddin Ashrafizadeh**: Methodology, Writing - review & editing, Supervision, Project administration. **Pranab Kumar Mondal**: Methodology, Writing - review & editing, Supervision.

References

1. Y. Liu, Y. Jian and C. Yang, *Energy*, 2020, **198**, 117401.https://doi.org/10.1016/j.energy.2020.117401
2. Z. Yang, Q. Meng, W. Yan, J. Lv, Z. Guo, X. Yu, Z. Chen, T. Guo and R. Zeng, *Energy*, 2015, **82**, 960-967.https://doi.org/10.1016/j.energy.2015.01.105
3. T. Xiao, B. Lu, Z. Liu, Q. Zhang, J. Zhai and X. Diao, *Journal of Membrane Science*, 2022, **642**, 119999.https://doi.org/10.1016/j.memsci.2021.119999

4. W.-x. Li, Z. Yang, W.-l. Liu, Z.-h. Huang, H. Zhang, M.-p. Li, X.-h. Ma, C. Y. Tang and Z.-l. Xu, *Journal of Membrane Science*, 2021, **618**, 118681.https://doi.org/10.1016/j.memsci.2020.118681
5. R. Long, Z. Kuang, Z. Liu and W. Liu, *Journal of Membrane Science*, 2018, **561**, 1-9.https://doi.org/10.1016/j.memsci.2018.05.026
6. E. Whiddon, H. Zhu and X. Zhu, *Journal of Power Sources*, 2019, **435**, 226796.https://doi.org/10.1016/j.jpowsour.2019.226796
7. L. Ma, Z. Li, Z. Yuan, H. Wang, C. Huang and Y. Qiu, *Journal of Power Sources*, 2021, **492**, 229637.https://doi.org/10.1016/j.jpowsour.2021.229637
8. Z. Kuang, D. Zhang, Y. Shen, R. Long, Z. Liu and W. Liu, *Journal of Power Sources*, 2019, **418**, 33-41.https://doi.org/10.1016/j.jpowsour.2019.02.045
9. L. Wei, X. Z. Fan, H. R. Jiang, K. Liu, M. C. Wu and T. S. Zhao, *Journal of Power Sources*, 2020, **478**, 228725.https://doi.org/10.1016/j.jpowsour.2020.228725
10. G. R. Iglesias, S. Ahualli, A. V. Delgado, P. M. Arenas-Fernández and M. M. Fernández, *Journal of Power Sources*, 2020, **453**, 227840.https://doi.org/10.1016/j.jpowsour.2020.227840
11. G. Laucirica, A. G. Albesa, M. E. Toimil-Molares, C. Trautmann, W. A. Marmisollé and O. Azzaroni, *Nano Energy*, 2020, **71**, 104612.https://doi.org/10.1016/j.nanoen.2020.104612
12. R. Sarma, A. K. Shukla, H. S. Gaikwad, P. K. Mondal and S. Wongwises, *Journal of Thermal Analysis and Calorimetry*, 2020, 1-16.https://doi.org/10.1007/s10973-020-10341-6
13. H. S. Gaikwad, A. Roy, P. K. Mondal, N. Chimres and S. Wongwises, *Analytica Chimica Acta*, 2019, **1045**, 85-97.https://doi.org/10.1016/j.aca.2018.08.058
14. H. S. Gaikwad, P. K. Mondal and S. Wongwises, *Scientific Reports*, 2018, **8**, 7893.https://doi.org/10.1038/s41598-018-26056-6
15. M. Khosravikia and A. Rahbar-Kelishami, *Journal of Molecular Liquids*, 2022, **358**, 119210.https://doi.org/10.1016/j.molliq.2022.119210
16. M. Khatibi, S. N. Ashrafizadeh and A. Sadeghi, *Analytica Chimica Acta*, 2020, **1122**, 48-60.https://doi.org/10.1016/j.aca.2020.05.011
17. M. Karimzadeh, Z. Seifollahi, M. Khatibi and S. N. Ashrafizadeh, *Electrochimica Acta*, 2021, **399**, 139376.https://doi.org/10.1016/j.electacta.2021.139376
18. X. Huang, Z. Zhang, X.-Y. Kong, Y. Sun, C. Zhu, P. Liu, J. Pang, L. Jiang and L. Wen, *Nano Energy*, 2019, **59**, 354-362.https://doi.org/10.1016/j.nanoen.2019.02.056
19. R. Long, Z. Kuang, Z. Liu and W. Liu, *Physical Chemistry Chemical Physics*, 2018, **20**, 7295-7302. https://doi.org/10.1039/C7CP08394G
20. A. Alinezhad, M. Khatibi and S. Nezameddin Ashrafizadeh, *Journal of Molecular Liquids*, 2021, 118324.https://doi.org/10.1016/j.molliq.2021.118324
21. R. Sarma and P. K. Mondal, *Journal of Heat Transfer*, 2018, **140**.https://doi.org/10.1115/1.4038451
22. B. D. Kang, H. J. Kim, M. G. Lee and D.-K. Kim, *Energy*, 2015, **86**, 525-538.https://doi.org/10.1016/j.energy.2015.04.056
23. R. Long, B. Li, Z. Liu and W. Liu, *Journal of Membrane Science*, 2017, **525**, 107-115.https://doi.org/10.1016/j.memsci.2016.10.035
24. B. E. Logan and M. Elimelech, *Nature*, 2012, **488**, 313-319.https://doi.org/10.1038/nature11477

25. C.-Y. Lin, F. Chen, L.-H. Yeh and J.-P. Hsu, *Physical Chemistry Chemical Physics*, 2016, **18**, 30160-30165.https://doi.org/10.1039/C6CP06459K
26. Y. Qi and M. C. McAlpine, *Energy & Environmental Science*, 2010, **3**, 1275-1285.https://doi.org/10.1039/C0EE00137F
27. J. Zhang, K. Zhan, S. Wang and X. Hou, *Soft matter*, 2020, **16**, 2915-2927.https://doi.org/10.1039/C9SM02506E
28. S. Chanda and P. A. Tsai, *Energy*, 2019, **176**, 531-543.https://doi.org/10.1016/j.energy.2019.03.136
29. F. Giacalone, M. Papapetrou, G. Kosmadakis, A. Tamburini, G. Micale and A. Cipollina, *Energy*, 2019, **181**, 532-547.https://doi.org/10.1016/j.energy.2019.05.161
30. S. Santoro, R. A. Tufa, A. H. Avci, E. Fontananova, G. Di Profio and E. Curcio, *Energy*, 2021, **228**, 120563.https://doi.org/10.1016/j.energy.2021.120563
31. Z. Seifollahi and S. N. Ashrafizadeh, *Colloids and Surfaces B: Biointerfaces*, 2022, **216**, 112545.https://doi.org/10.1016/j.colsurfb.2022.112545
32. R. Sarma, M. Jain and P. K. Mondal, *Physics of Fluids*, 2017, **29**, 103102.https://doi.org/10.1063/1.4991597
33. P. Kaushik, P. K. Mondal and S. Chakraborty, *Microfluidics and Nanofluidics*, 2017, **21**, 122.https://doi.org/10.1007/s10404-017-1957-9
34. H. Gaikwad, D. N. Basu and P. K. Mondal, *ELECTROPHORESIS*, 2016, **37**, 1998-2009.https://doi.org/10.1002/elps.201500457
35. L. Cao, F. Xiao, Y. Feng, W. Zhu, W. Geng, J. Yang, X. Zhang, N. Li, W. Guo and L. Jiang, *Advanced Functional Materials*, 2017, **27**, 1604302.https://doi.org/10.1002/adfm.201604302
36. Z. Hu, L. Zhang, J. Huang, Z. Feng, Q. Xiong, Z. Ye, Z. Chen, X. Li and Z. Yu, *Nanoscale*, 2021, **13**, 8264-8274.https://doi.org/10.1039/D1NR00169H
37. R. Wang, C. He, W. Chen, L. Fu, C. Zhao, J. Huo and C. Sun, *Nanoscale*, 2021, **13**, 19247-19254.https://doi.org/10.1039/D1NR06366A
38. A. A. Moya, *Electrochimica Acta*, 2017, **238**, 134-141.https://doi.org/10.1016/j.electacta.2017.04.022
39. Y. Ma, L.-H. Yeh, C.-Y. Lin, L. Mei and S. Qian, *Analytical chemistry*, 2015, **87**, 4508-4514.https://doi.org/10.1021/acs.analchem.5b00536
40. M. Monesi, M. Khatibi and A. Rahbar-Kelishami, *Scientific Reports*, 2022, **12**, 12170.https://doi.org/10.1038/s41598-022-16482-y
41. M. Wang, W. Shen, S. Ding, X. Wang, Z. Wang, Y. Wang and F. Liu, *Nanoscale*, 2018, **10**, 18821-18828.https://doi.org/10.1039/C8NR04962A
42. X. Liu, M. He, D. Calvani, H. Qi, K. B. S. S. Gupta, H. J. M. de Groot, G. J. A. Sevink, F. Buda, U. Kaiser and G. F. Schneider, *Nature nanotechnology*, 2020, **15**, 307-312.https://doi.org/10.1038/s41565-020-0641-5
43. H.-C. Yeh, C.-C. Chang and R.-J. Yang, *RSC Advances*, 2014, **4**, 2705-2714.https://doi.org/10.1039/C3RA45392H
44. D.-K. Kim, C. Duan, Y.-F. Chen and A. Majumdar, *Microfluidics and Nanofluidics*, 2010, **9**, 1215-1224.https://doi.org/10.1007/s10404-010-0641-0
45. J. Kim, S. J. Kim and D.-K. Kim, *Energy*, 2013, **51**, 413-421.https://doi.org/10.1016/j.energy.2013.01.019
46. G. Pérez-Mitta, W. A. Marmisolle, L. Burr, M. E. Toimil-Molares, C. Trautmann and O. Azzaroni, *Small*, 2018, **14**, 1703144.https://doi.org/10.1002/smll.201703144

47. G. Pérez-Mitta, W. A. Marmisollé, A. G. Albesa, M. E. Toimil-Molares, C. Trautmann and O. Azzaroni, *Small*, 2018, **14**, 1702131.https://doi.org/10.1002/smll.201702131
48. G. Pérez-Mitta, W. A. Marmisollé, C. Trautmann, M. E. Toimil-Molares and O. Azzaroni, *Advanced Materials*, 2017, **29**, 1700972.https://doi.org/10.1002/adma.201700972
49. G. Laucirica, W. A. Marmisollé, M. E. Toimil-Molares, C. Trautmann and O. Azzaroni, *ACS applied materials & interfaces*, 2019, **11**, 30001-30009.https://doi.org/10.1021/acsami.9b05961
50. G. Pérez-Mitta, M. E. Toimil-Molares, C. Trautmann, W. A. Marmisollé and O. Azzaroni, *Advanced Materials*, 2019, **31**, 1901483. https://doi.org/10.1002/adma.201901483
51. B. Yameen, M. Ali, R. Neumann, W. Ensinger, W. Knoll and O. Azzaroni, *Journal of the American Chemical Society*, 2009, **131**, 2070-2071.https://doi.org/10.1021/ja8086104
52. A. Sadeghi, *Microfluidics and Nanofluidics*, 2021, **25**, 1-23.https://doi.org/10.1007/s10404-021-02444-9
53. S. Ayoubi, M. Khatibi and S. N. Ashrafizadeh, *Microfluidics and Nanofluidics*, 2021, **25**.http://doi.org/10.1007/s10404-021-02501-3
54. A. Sadeghi, *Journal of Fluid Mechanics*, 2019, **862**, 517-551.https://doi.org/10.1017/jfm.2018.979
55. P. Kaushik, P. K. Mondal, P. K. Kundu and S. Wongwises, *Physics of Fluids*, 2019, **31**, 022009.https://doi.org/10.1063/1.5086327
56. H. S. Gaikwad, G. Kumar and P. K. Mondal, *Soft Matter*, 2020, **16**, 6304-6316.https://doi.org/10.1039/D0SM00890G
57. S. R. Gorthi, H. S. Gaikwad, P. K. Mondal and G. Biswas, *Industrial & Engineering Chemistry Research*, 2020, **59**, 3839-3853.https://doi.org/10.1021/acs.iecr.9b00767
58. L.-X. Zhang, S.-L. Cai, Y.-B. Zheng, X.-H. Cao and Y.-Q. Li, *Advanced Functional Materials*, 2011, **21**, 2103-2107.https://doi.org/10.1002/adfm.201002627
59. S. Umehara, N. Pourmand, C. D. Webb, R. W. Davis, K. Yasuda and M. Karhanek, *Nano Letters*, 2006, **6**, 2486-2492.https://doi.org/10.1021/nl061681k
60. X. L. Deng, T. Takami, J. W. Son, E. J. Kang, T. Kawai and B. H. Park, *Scientific Reports*, 2014, **4**, 4005.https://doi.org/10.1038/srep04005
61. S. Liu, Y. Dong, W. Zhao, X. Xie, T. Ji, X. Yin, Y. Liu, Z. Liang, D. Momotenko, D. Liang, H. H. Girault and Y. Shao, *Analytical Chemistry*, 2012, **84**, 5565-5573.https://doi.org/10.1021/ac3004852
62. M. Khatibi, A. Sadeghi and S. N. Ashrafizadeh, *Physical Chemistry Chemical Physics*, 2021, **23**, 2211-2221.https://doi.org/10.1039/D0CP05974A
63. M. Khatibi, S. N. Ashrafizadeh and A. Sadeghi, *Electrochimica Acta*, 2021, **395**, 139221.https://doi.org/10.1016/j.electacta.2021.139221
64. R. Long, Z. Kuang, Z. Liu and W. Liu, *National Science Review*, 2019, **6**, 1266-1273.https://doi.org/10.1093/nsr/nwz106
65. R. Long, F. Wu, X. Chen, Z. Liu and W. Liu, *International Journal of Heat and Mass Transfer*, 2021, **168**, 120842.https://doi.org/10.1016/j.ijheatmasstransfer.2020.120842
66. W. Zhang, Q. Wang, M. Zeng and C. Zhao, *International Journal of Heat and Mass Transfer*, 2019, **143**, 118569.https://doi.org/10.1016/j.ijheatmasstransfer.2019.118569

67. C. Qi and C.-O. Ng, *International Journal of Heat and Mass Transfer*, 2018, **119**, 52-64.https://doi.org/10.1016/j.ijheatmasstransfer.2017.11.114
68. R. Long, Z. Luo, Z. Kuang, Z. Liu and W. Liu, *Nano Energy*, 2020, **67**, 104284.https://doi.org/10.1016/j.nanoen.2019.104284
69. M. Karimzadeh, M. Khatibi and S. N. Ashrafizadeh, *International Communications in Heat and Mass Transfer*, 2021, **129**, 105728.https://doi.org/10.1016/j.icheatmasstransfer.2021.105728
70. J. Huo, L. Fu, C. Zhao and C. He, *Chinese Chemical Letters*, 2021.https://doi.org/10.1016/j.cclet.2020.12.059
71. A. Würger, *Reports on Progress in Physics*, 2010, **73**, 126601.https://doi.org/10.1088/0034-4885/73/12/126601
72. J. Zhong and C. Huang, *International Journal of Heat and Mass Transfer*, 2020, **152**, 119501.https://doi.org/10.1016/j.ijheatmasstransfer.2020.119501
73. J. Zhong and C. Huang, *Langmuir*, 2020, **36**, 1418-1422.https://doi.org/10.1021/acs.langmuir.9b03141
74. L. A. Bromley, *AIChE Journal*, 1973, **19**, 313-320. https://doi.org/10.1002/aic.690190216
75. T. Ghonge, J. Chakraborty, R. Dey and S. Chakraborty, *Physical Review E*, 2013, **88**, 053020.https://doi.org/10.1103/PhysRevE.88.053020
76. F. Römer, Z. Wang, S. Wiegand and F. Bresme, *The Journal of Physical Chemistry B*, 2013, **117**, 8209-8222.https://doi.org/10.1021/jp403862x
77. J. C. Fair and J. F. Osterle, *The Journal of Chemical Physics*, 1971, **54**, 3307-3316.https://doi.org/10.1063/1.1675344
78. J.-P. Hsu, T.-C. Su, C.-Y. Lin and S. Tseng, *Electrochimica Acta*, 2019, **294**, 84-92.https://doi.org/10.1016/j.electacta.2018.10.074
79. J.-P. Hsu, S.-C. Lin, C.-Y. Lin and S. Tseng, *Journal of Power Sources*, 2017, **366**, 169-177.https://doi.org/10.1016/j.jpowsour.2017.09.022
80. C. Li, Z. Liu, H. Zhang, N. Qiao, Z. Zhang, J. Zhou and Z. Q. Tian, *International Communications in Heat and Mass Transfer*, 2022, **135**, 106121.https://doi.org/10.1016/j.icheatmasstransfer.2022.106121